Supplementary information

Facile development of microstructure-engineered, ligand-chelated SiO_2-ZrO_2 composite membranes for molecular separations

Sulaiman Oladipo Lawal, Hiroki Nagasawa, Toshinori Tsuru, and Masakoto Kanezashi*

Department of Chemical Engineering, Graduate School of Engineering, Hiroshima University, 1-4-1 Kagamiyama, Higashi-Hiroshima 739-8527, Japan

*Corresponding author: E-mail address: kanezashi@hiroshima-u.ac.jp (M. Kanezashi)

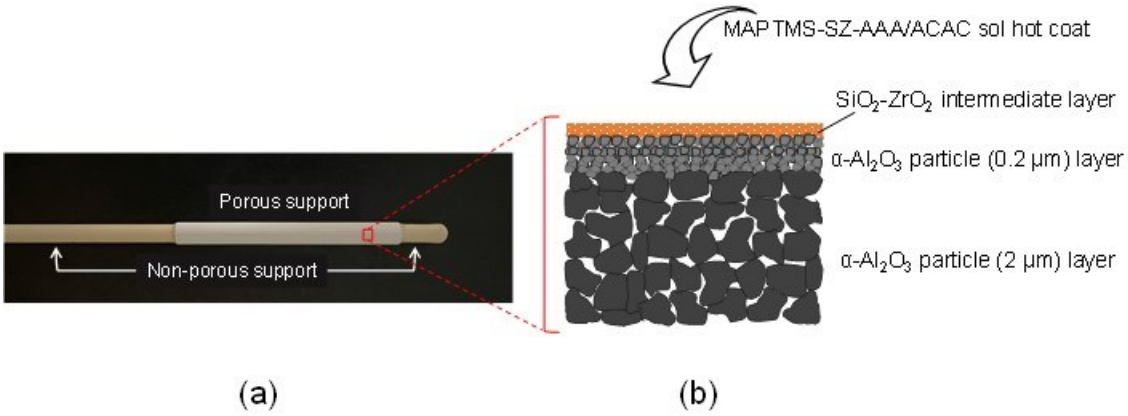

Fig. S1 (a) Picture of a membrane module comprised of porous and non-porous sections (b) schematic diagram describing the cross-sectional morphology of the prefabricated support structure prior to forming the active top layer.

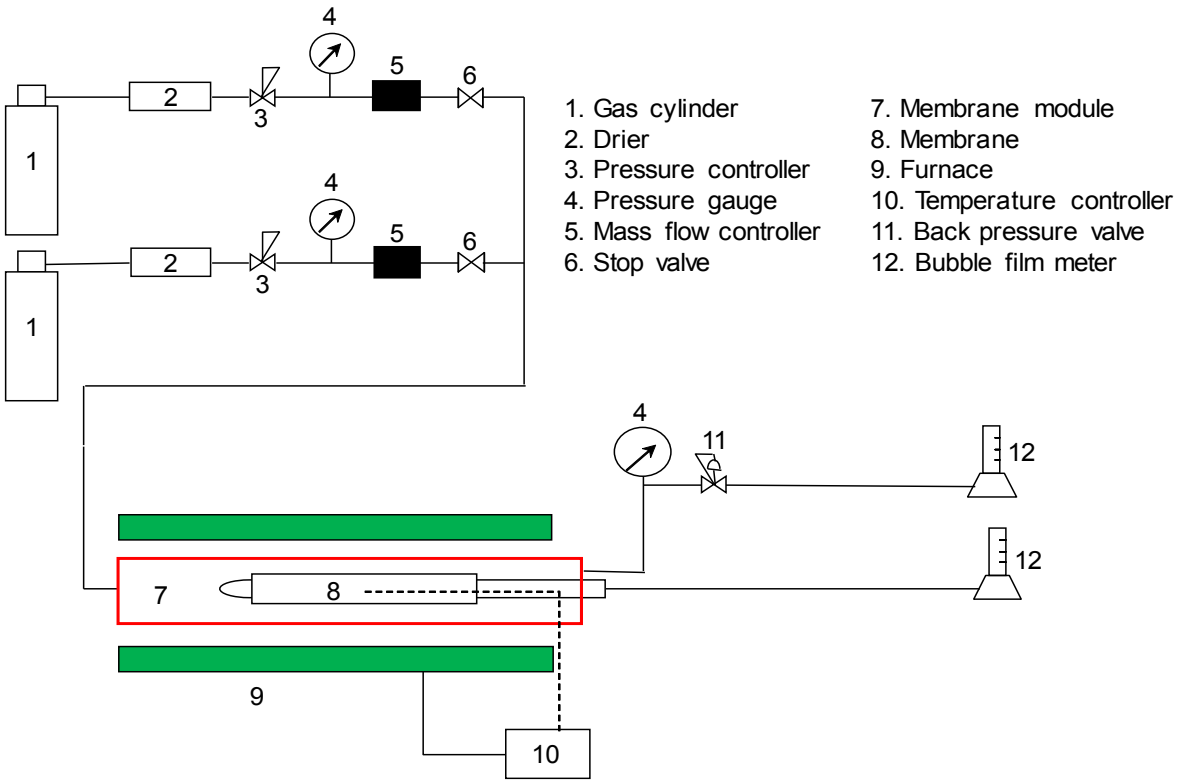

Fig. S2 Schematic process flow diagram of the gas permeation testing setup (test pressures: P_u = 200, P_d = 100 kPa (a)).

Figure S3 shows the sol size measured by intensity, which served as a primary basis for obtaining the polysispersity index and z-average values. From Figure S3 it is evident that the sol sizes of sols increased dramatically on the order of 10^2-10^3 nm when AIBN was added. However, the control of sols subjected to similar reaction conditions with the AIBN-containing sols showed no change compared with the pre-prepared sols.

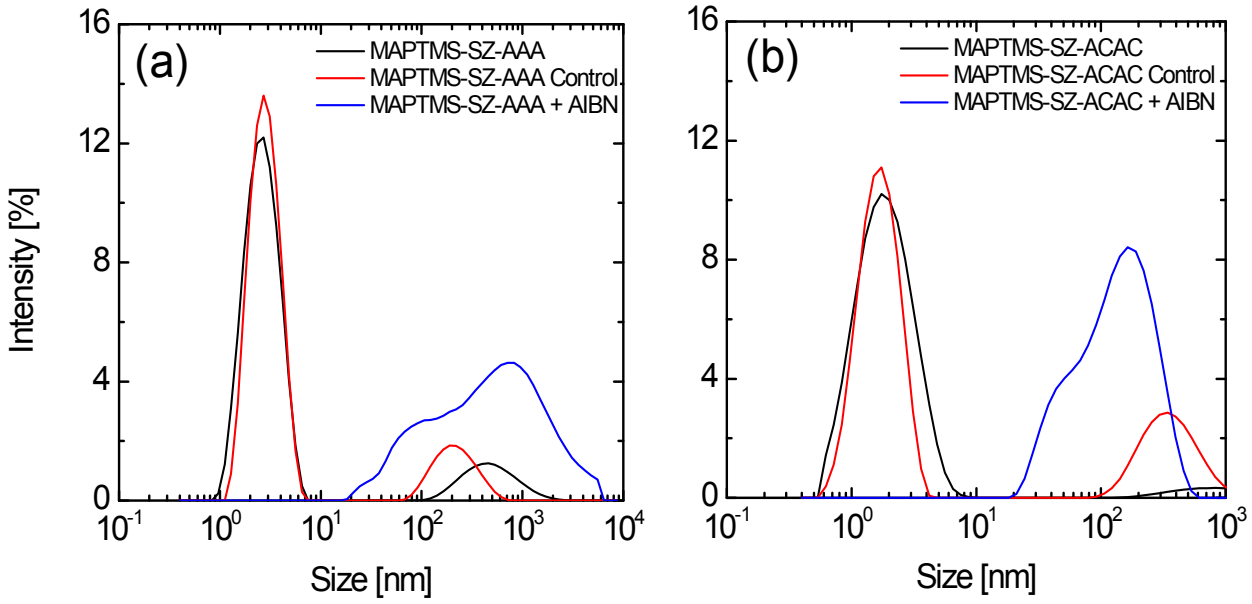

Fig. S3 Sol size based on intensity measured at room temperature for pre-prepared, control and AIBN-containing (a) MAPTMS-SZ-AAA and (b) MAPTMS-SZ-ACAC sols.

Since sol size of AIBN-containing sols are very large and hence difficult to fabricate membranes with, it is important to thin down the particle size to suitable ranges for membrane preparation. P-xylene was successfully utilized to achieve this. Figure S4(a) shows the sol size by number of the p-xylene-dissolved sols and shows that the sol size can indeed be controlled to within 2 and 8 nm. To explain the dissolution process, consider Figure S4(b). Prior to addition of p-xylene solvent, the crosslink chains are densely packed and therefore, the light scattering is severe in this case. After the addition of p-xylene, the solute-solute interaction between the chains become broken and overtaken by solvent-solute interactions and the chains become scattered in the solvent. In this case, the light scattering ability will be greatly reduced hence registering a smaller sol size.

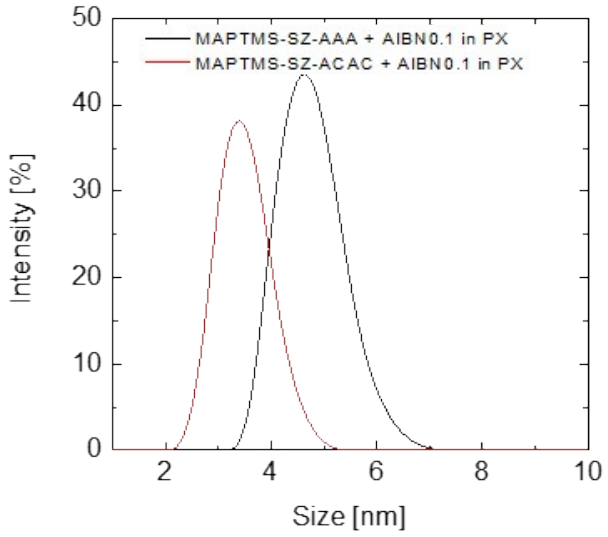

Fig. S4(a) Sol size based on number measured at room temperature for AIBN-containing MAPTMS-SZ-AAA and MAPTMS-SZ-ACAC sols dispersed in p-xylene.

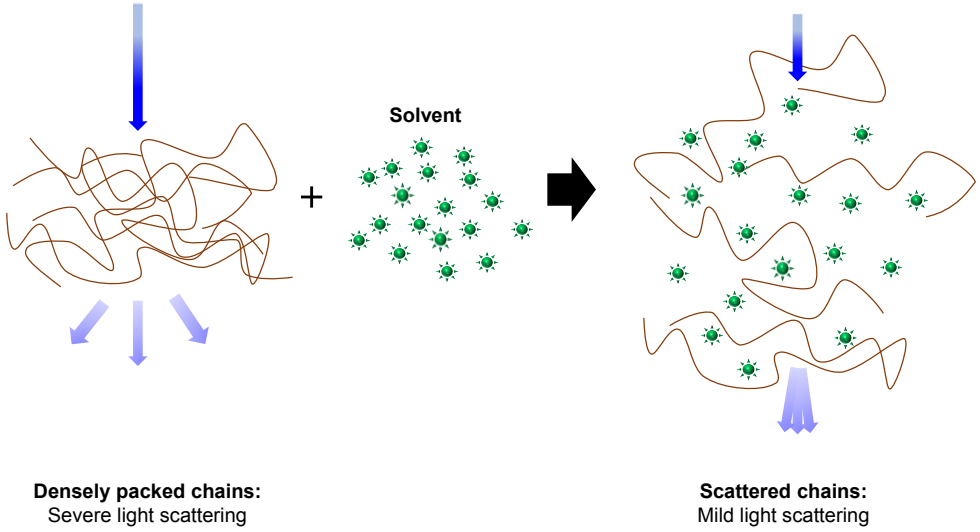

Fig. S4(b) Schematic image of the dissolution process of crosslinked samples in p-xylene.

Figures S5a and S5b show the observed FTIR profiles of as-prepared MAPTMS-SZ-AAA and MAPTMS-SZ-ACAC films, respectively, with different AIBN/C=C ratios ranging from 2500-500 cm^{-1}. The advancement of polymerization reactions were confirmed by the disappearance of C=C peaks (1638-1640, 1325 cm^{-1}) belonging to MAPTMS due to the organic crosslinking, the broadening and shift of the C=O peaks (1700-1720 cm^{-1}) of MAPTMS to a higher wave number due to the loss of conjugation with C=C and the broadening and shift of the peak representative of ligand chelation to zirconium (AAA: 1287 cm^{-1}, ACAC: 1280 cm^{-1}) in the case where a co-polymerization occurs between MAPTMS and a ligand. In addition, for an AIBN/C=C ratio of 1, free AIBN can be observed in the spectrum indicating that a saturation point was passed.

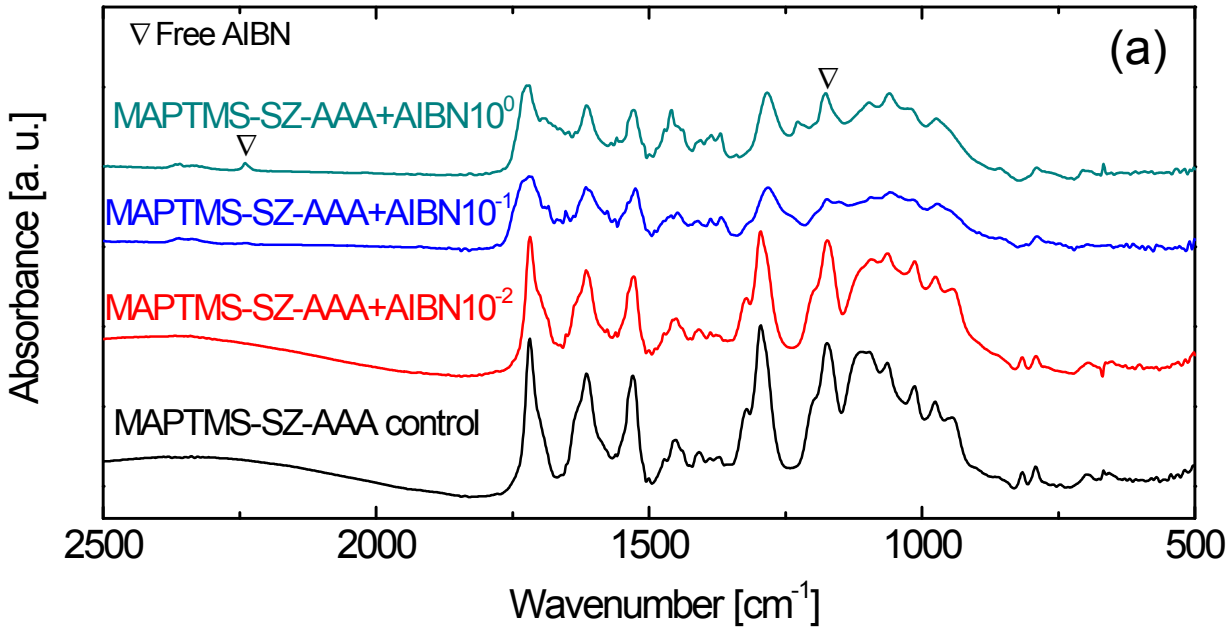

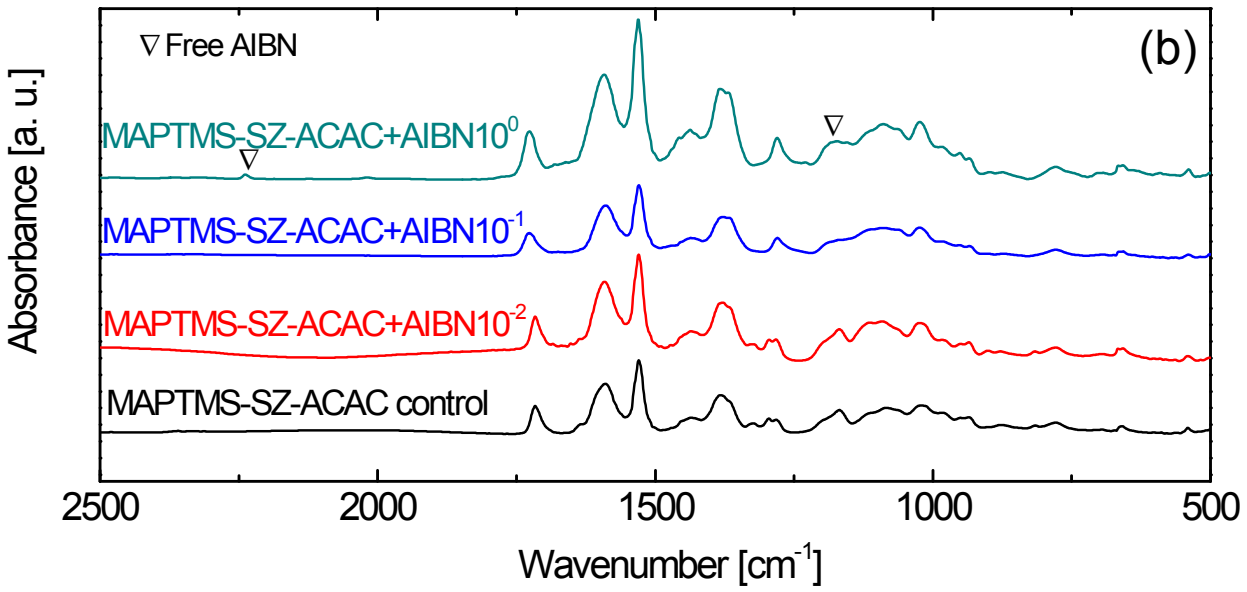

Fig. S5 Observed FTIR spectra presented in the wavenumber range of 2,500 to 500 cm^{-1} for films prepared from (a) MAPTMS-SZ-AAA and (b) MAPTMS-SZ-ACAC polymerized with different AIBN/C=C ratios.

Figures S6a and S6b show the measured XRD patterns of MAPTMS-SZ-AAA and MAPTMS-SZ-ACAC powders, respectively, with different AIBN/C=C ratios (0, 0.01, 0.1, 1). The observance of XRD patterns is important to examine the effect of organic crosslinking on the lattice framework of the materials. Considering Bragg's law ($n\lambda = 2dsin\theta$; where n is a positive integer, λ is the wavelength of the incident x-rays, d is the spacing between successive lattice layers, and θ is the glancing angle of incidence) for an ordered lattice, the product $2dsin\theta$ results in a whole number multiple of the x-ray wavelength λ since the lattice spacing, d, is equal throughout the material structure. For a disordered lattice, however, d is different throughout the

material structure making the value of $2dsin\theta$ not a whole number multiple of the x-ray wavelength, λ. [1] This will result in the production of poorly defined basal reflections. [2] As shown in both Figures S6a and S6b, as the AIBN/C=C ratio increases, the XRD patterns become more flattened and less defined.

In the work of Chen *et al.* [3] concerning the *in-situ* bulk polymerization of methyl methacrylate (MMA) in layered double hydroxides (LDHs) to form a LDH/PMMA composite, as the conversion of MMA monomers increased, the observed XRD peaks became more flattened and less defined as a result of random dispersion and disorder of the LDHs in the formed PMMA matrix. Consequently, we concluded that the increased conversion of the C=C bonds due to organic crosslinking as the AIBN/C=C ratio increased caused a disorderly dispersion of the inorganic silica-zirconia matrix leading to poorly defined XRD patterns. This phenomenon was more evident in the AAA-chelated sample (Figure S6a) than in the ACAC-chelated sample (Figure S6b), an effect that can be attributed to the difference in the organic crosslinking nature in both systems. It is worth noting that the broader spectra observed for AAA-chelated samples may be due to improper overlap of the individual spectra of the siloxane and zirconium oxide networks since the chelation chemistries of AAA and ACAC to zirconium are different. [4]

In addition, the amorphous structure of the samples was confirmed by transmission electron micrography (TEM). Figures S6c and S6d show the TEM images of CL-AAA and CL-ACAC samples taken at a scale of 5 nm. Both images display no aggregation of particles associated with crystalline structures.

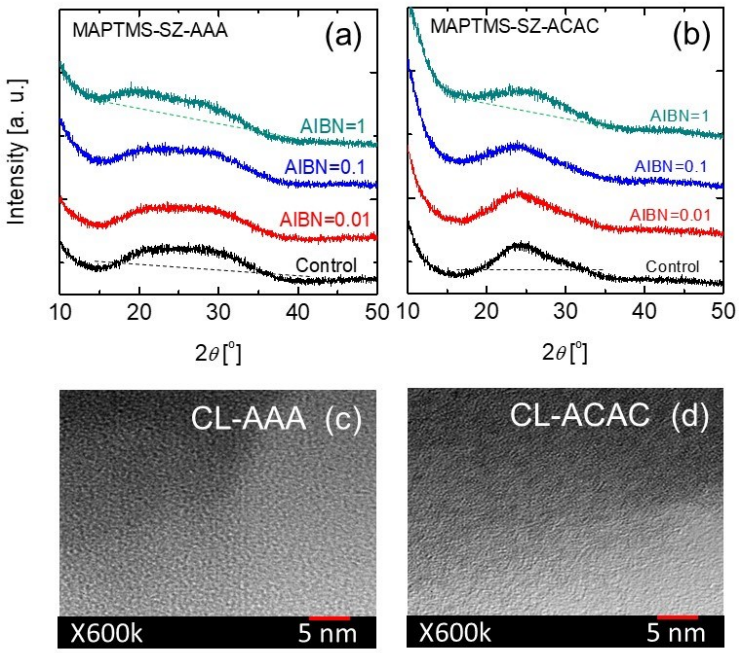

Fig. S6 Observed XRD diffractograms of as-prepared (a) MAPTMS-SZ-AAA and (b) MAPTMS-SZ-ACAC powders, respectively, with different AIBN/C=C ratios (0, 0.01, 0.1, and 1) measured at room temperature presented in a 2θ range of 10-50°. Observed TEM images of (c) crosslinked MAPTMS-SZ-AAA and (c) crosslinked MAPTMS-SZ-ACAC films, respectively.

Figures S7a and S7b detail the CO_2 adsorption-desorption isotherms for all samples measured at 20, 25 and 30 °C. As expected, the amount of CO_2 adsorbed was reduced as measurement temperature increased. Also, organic crosslinked samples showed more CO_2 adsorbed compared with that of non-crosslinked samples. Figures S7c and S7d show the calculated isosteric heats of CO_2 adsorption using the isotherms in Figures S7a and S7b. The Clausius-Clapeyron equation was utilized in obtaining the values of CO_2 heat of adsorption at each CO_2 loading. The Clausius-Clapeyron equation is shown below.

$$\Delta Q_{st} = \frac{RT_1T_n}{T_n - T_1}\ln\frac{P_n}{P_1} \qquad \text{(S1)}$$

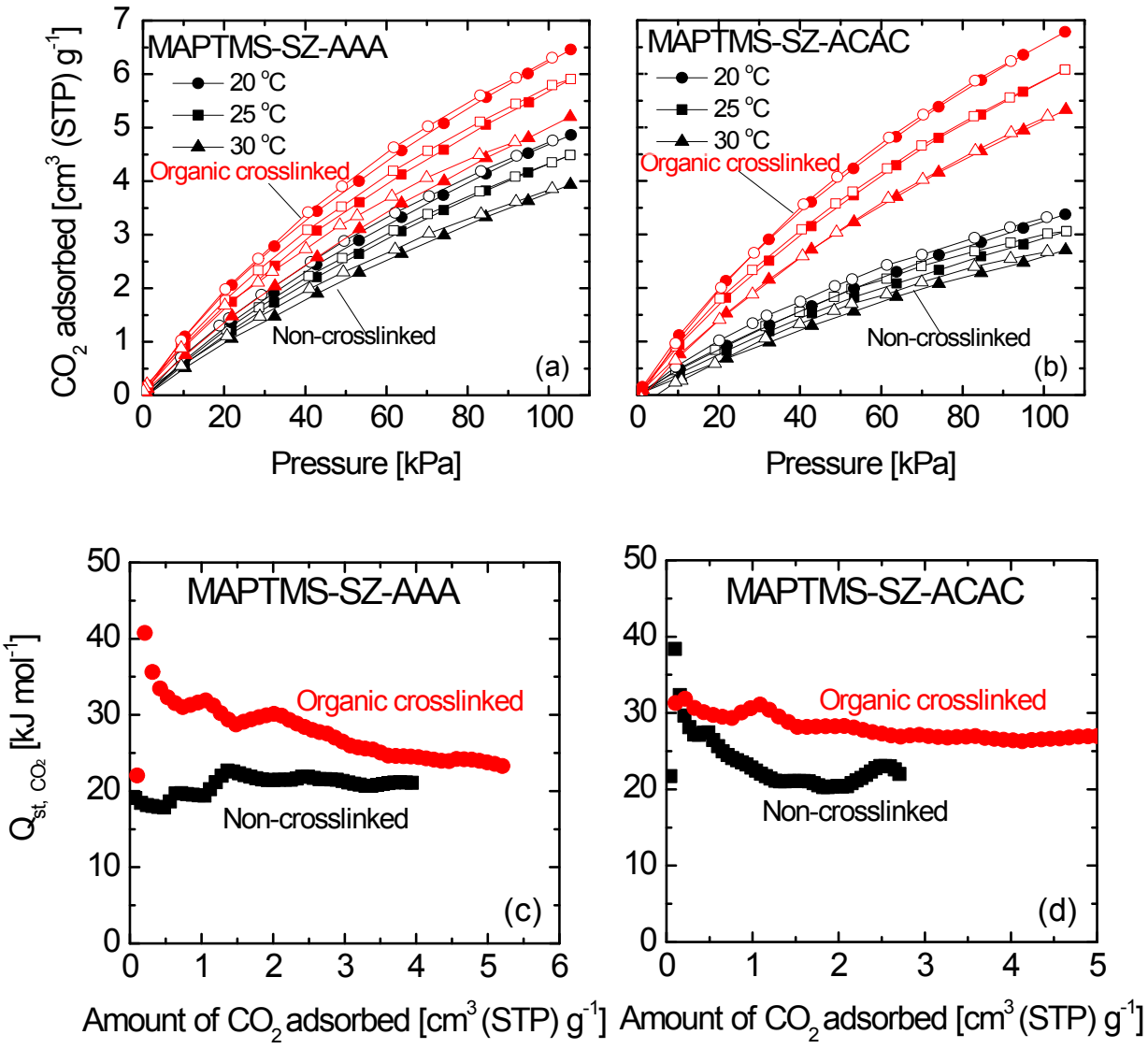

Fig. S7 CO_2 adsorption-desorption isotherms for non-crosslinked and organic cross-linked samples in (a) MAPTMS-SZ-AAA and (b) MAPTMS-SZ-ACAC measured at 20, 25 and 30 °C.

Corresponding isosteric values for heat of CO_2 adsorption plots calculated based on the Clausius-Clapeyron equation are presented in panels (c) and (d), respectively.

Figures S8a and S8b show the differential thermogravimetry (DTG) curves of powders from MAPTMS-SZ-AAA and MAPTMS-SZ-ACAC crosslinked with different AIBN/C=C ratios up to the final decomposition temperature. The thermal decomposition of materials occurred in two stages. The first stage occurred between 100 and 300 ^oC, as indicated by the DTG peak between 200 and 250 ^oC. This decomposition was assigned to the release of residual solvent, adsorbed moisture, and further condensation reactions. The second stage occurred from 300 ^oC when the organic contents started to decompose. Therefore, to fabricate membranes, 250 ^oC provides the optimum amount of heat needed to remove residual solvent and further the condensation reactions between silanol groups and unhydrolyzed alkoxide groups (-SiOH + -SiOH → -SiOSi- + H_2O or -SiOH + $-SiOCH_3$ → -SiOSi- + CH_3OH) but not enough to decompose the organic moieties.

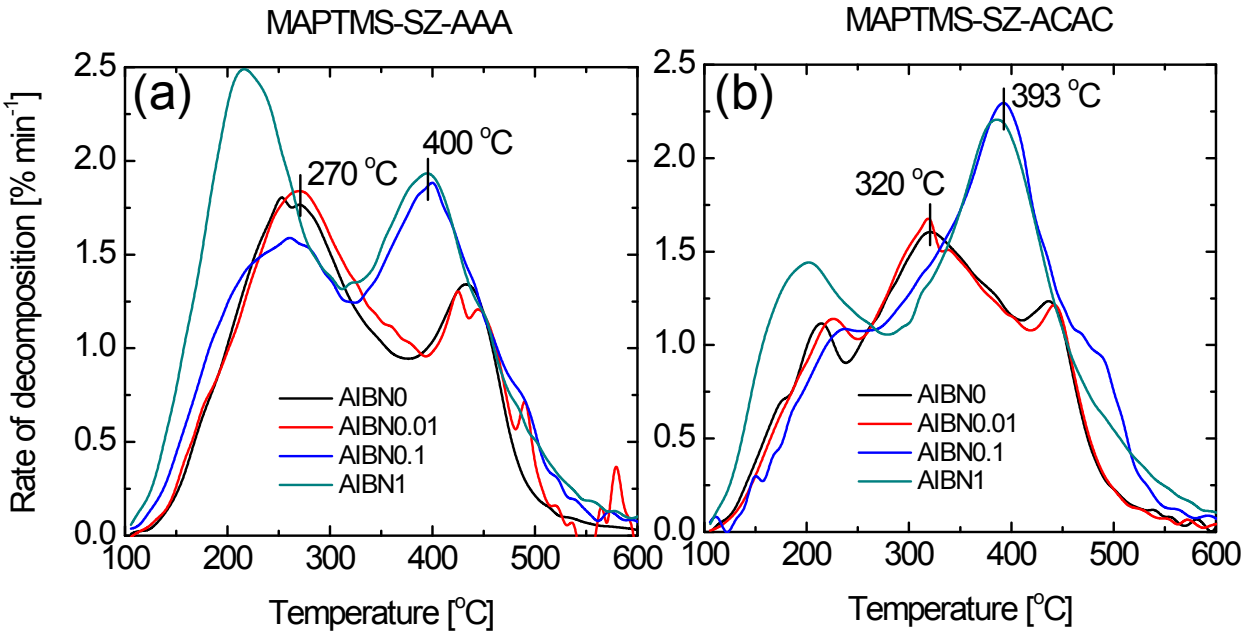

Fig. S8 Differential thermogravimetry curves of powders from (a) MAPTMS-SZ-AAA and (b) MAPTMS-SZ-ACAC crosslinked with different AIBN/C=C ratios up to the final decomposition temperature.

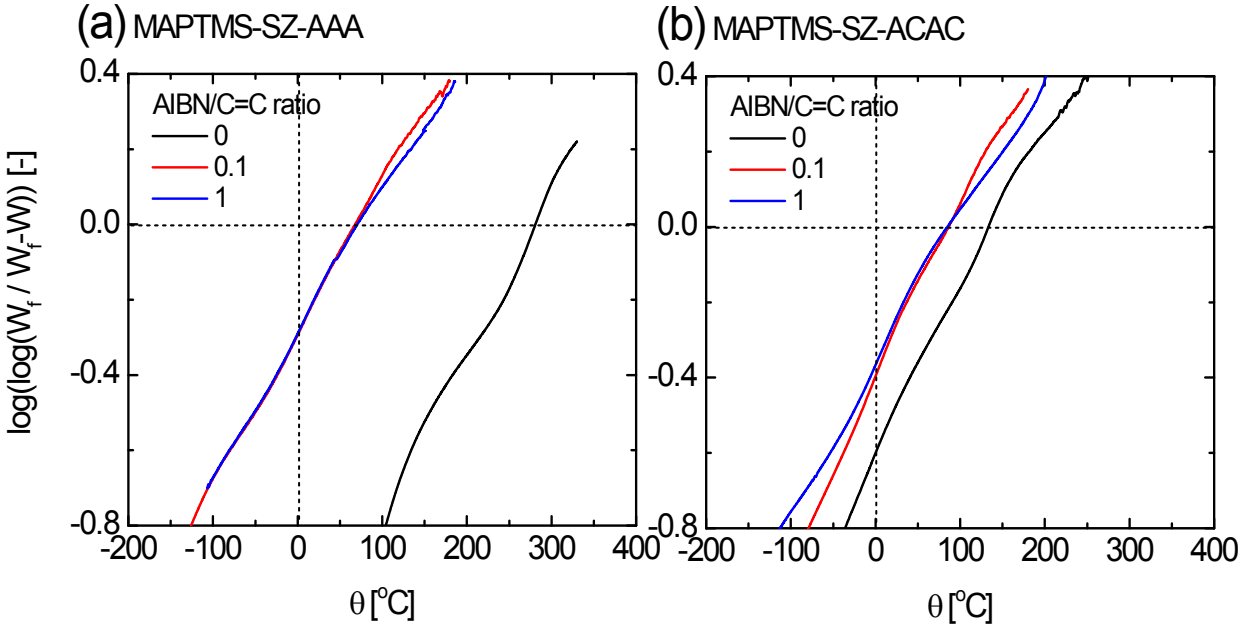

Figure S9 Plot of $log.\left[log\frac{W_f}{W_f - W}\right]$ against θ based on the Horowitz-Metzger equation (Equation 1) for (a) MAPTMS-SZ-AAA and (b) MAPTMS-SZ-ACAC powders derived from sols polymerized with different AIBN/C=C ratios.

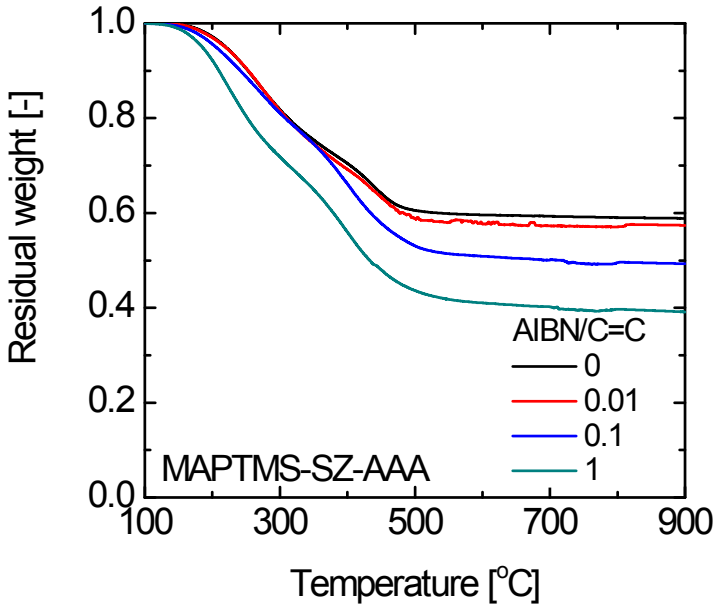

Fig. S10 Thermogravimetry (TGA) curves of MAPTMS-SZ-AAA samples with different AIBN/C=C ratios fired under a N_2 atmosphere.

The modified gas translation model proposed by Lee *et al.* [5] presents a way to estimate the mean pore size of membranes with pore size of less than 1 nm by employing an NKP (normalized Knudsen permeance) method based on the modified gas translation model expressed below.

$$P_i = \frac{1}{3\tau L}\frac{\varepsilon}{(d_p - d_i)}\frac{(d_p - d_i)^2}{d_p^2}\sqrt{\frac{8}{\pi M_i RT}}exp\left(-\frac{E_{p,i}}{RT}\right) \quad \text{(S2)}$$

$$P_i = \frac{k_{0,i}}{\sqrt{M_i RT}}exp\left(-\frac{E_{p,i}}{RT}\right) \quad \text{(S3)}$$

Where $\frac{\varepsilon}{3\tau L}\frac{(d_p - d_i)^3}{d_p^2}\sqrt{\frac{8}{\pi}}$ is the pre-exponential factor $k_{0,i}$ expressing the combination of configurational factors of the membrane and permeating molecule (porosity ε, tortuosity τ, membrane thickness L, mean pore diameter d_p and kinetic diameter d_i), $E_{p,i}$ is the apparent activation energy of permeation for a gas species, *i*, M_i is the molecular weight of the gas species, R is the universal gas constant and T is the permeation temperature. The NKP is the ratio of experimentally obtained permeance of *i* to the Knudsen permeance of *i* that can be expected based on a standard gas. In combination with Equation S2 and applying further simplifications, the mean pore diameter, d_p, can be estimated at any permeance temperature, T, using Equation S4 expressed as a function of the kinetic diameter, d_i, and employing d_p as the fitting parameter.

$$f_{NKP} = \frac{P_i}{P_s}\sqrt{\frac{M_i}{M_S}} \approx \frac{\left(1 - \frac{d_i}{d_p}\right)^3}{\left(1 - \frac{d_s}{d_p}\right)^3} \quad \text{(S4)}$$

Where S represents the standard gas.

The modified gas translation model was also used to estimate the mean pore size of membranes by employing the apparent activation energy of gas permeation, E_p, and a pre-exponential factor, k_0, of a gaseous species, *i*, as expressed in Equation S3. Equation S3 was then further simplified to give Equation S5.

$$k_{0,i}^{1/3} = a^{1/3}d_p - a^{1/3}d_i \quad \text{(S5)}$$

In Equation S5, a denotes a constant that depends only on the structure of the membrane. To estimate the mean pore diameter of each membrane, $k_{0,i}^{1/3}$ was plotted as a function of the kinetic diameter, d_i, of a gaseous species, i, using Equation S5, as shown in Figures S11a and S11b. A linear fitting of the plotted points for all the gaseous species in all the membranes can be established and the value of the mean pore size, d_p, is taken as the intercept on the x-axis. As is evident from the plots the mean pore diameters of organic crosslinked samples-derived membranes (OCL-AAA: 0.49 nm; OCL-ACAC: 0.53 nm) are considerably smaller than those of the non-crosslink-derived membranes (NCL-AAA: 0.76 nm; NCL-ACAC: 0.84 nm). Thus, the lower permeance values observed for organic crosslink-derived membranes resulted from the smaller pore size generated by the organic crosslinked network.

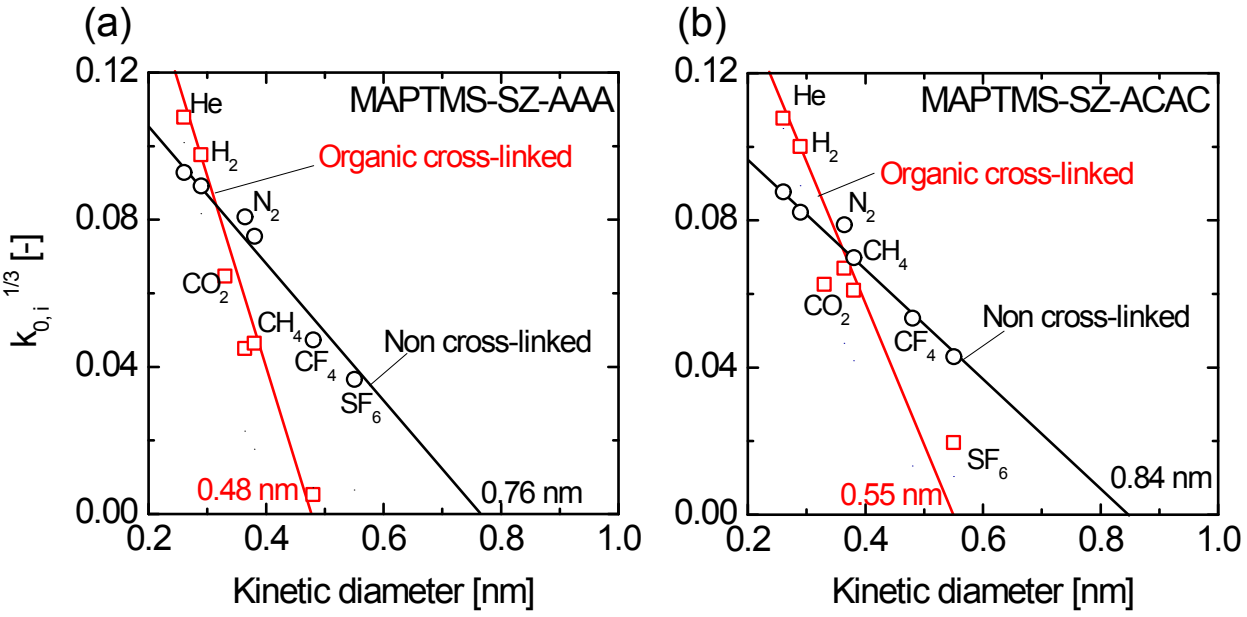

Fig. S11 Relationship between $k_{0,i}^{1/3}$ and kinetic diameter for (a) non-crosslinked and organic crosslinked MAPTMS-SZ-AAA and (b) non-crosslinked and organic crosslinked MAPTMS-SZ-ACAC.

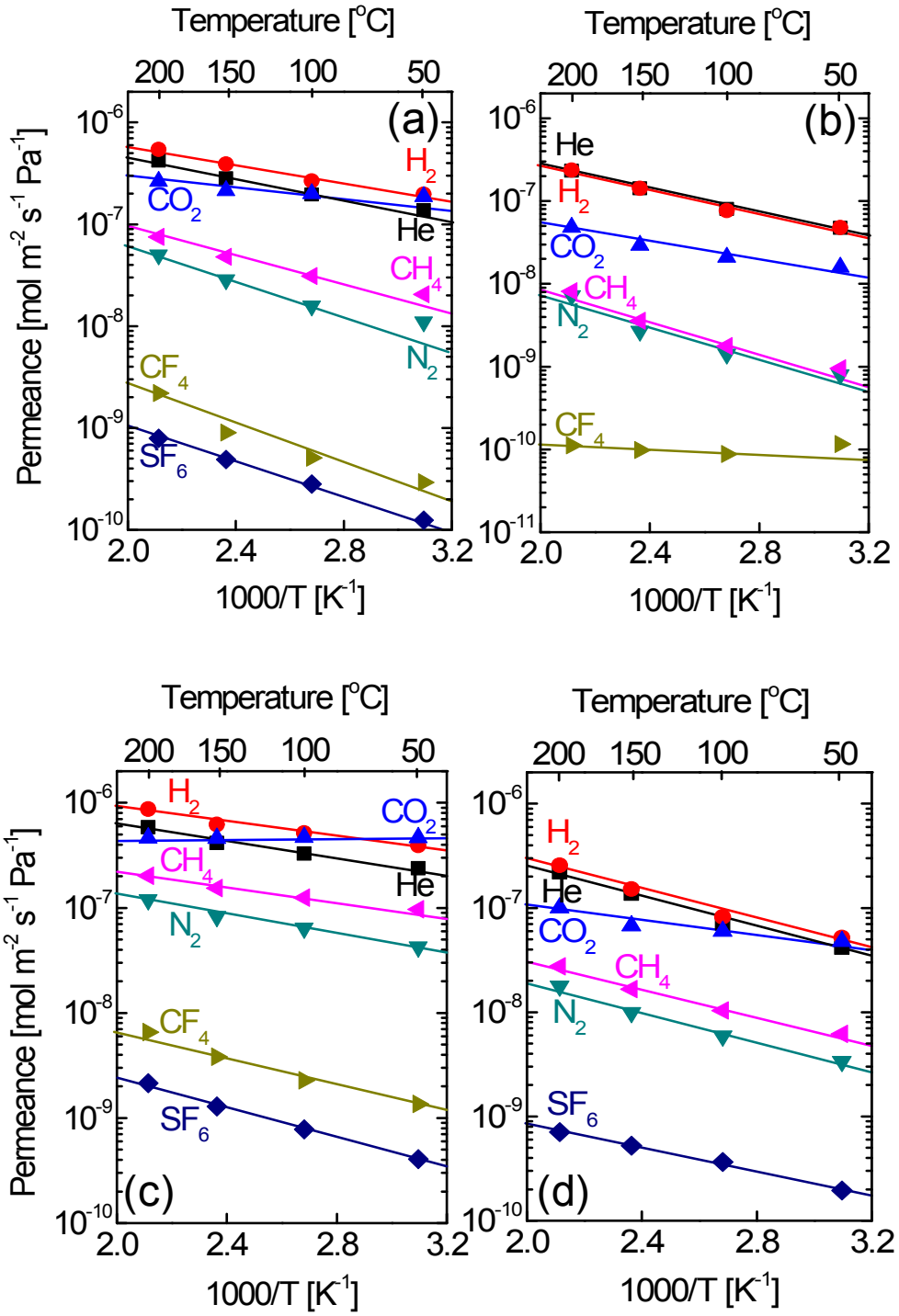

Fig. S12 Plots of the temperature dependence of single-gas permeance for membranes derived from (a) non-crosslinked MAPTMS-SZ-AAA, (b) organic crosslinked MAPTMS-SZ-AAA, (c) non-crosslinked MAPTMS-SZ-ACAC, and (d) organic crosslinked MAPTMS-SZ-ACAC.

Table S1 Estimated values of the apparent activation energies of gas permeance for different gases obtained from Figure S11

Membrane	$E_{p,\,i}$ [kJ mol^{-1}]						
	He	H_2	CO_2	N_2	CH_4	CF_4	SF_6
NCL-AAA	10.8	10.5	4.3	14.0	12.5	18.1	17.2
OCL-AAA	14.9	15.2	10.7	17.5	16.5	1.4	-
NCL-ACAC	9.0	8.1	1.5	11.0	7.7	14.8	15.5
OCL-ACAC	15.1	15.1	7.4	16.0	14.0	-	10.5

Table S2 Estimated values of $k_{0,\,i}$ for different gases obtained from Figure S11

Membrane	$k_{0,\,i}$ x 10^{-5} [-]						
	He	H_2	CO_2	N_2	CH_4	CF_4	SF_6
NCL-AAA	79.0	70.0	30.7	52.0	42.3	10.4	4.8
OCL-AAA	125.6	93.1	27.0	9.1	1.0	0.0	-
NCL-ACAC	70.0	59.0	27.9	49.0	34.1	15.3	8.0
OCL-ACAC	125.0	100.2	24.5	30.0	22.7	-	0.8

Supplementary reference(s)

(1) G. N. Eby, *Brooks/Cole-Thomson Learning*. 2004, 212-214

(2) R. A. Vaia, R. K. D. Jandt, E. J. Kramer, and E. P. Giannelis, *Chem. Mater.* 1996, **8** (11), 2628

(3) G. -A. Wang, C. -C. Wang, and C. -Y. Chen, *Polymer.* 2005, **46**, 5065-5074

(4) D. Hoebbel, T. Reinert, and H. Schmidt, *J. Sol-Gel Sci. Technol*. 1997, **10**, 115-126

(5) H. R. Lee, M. Kanezashi, Y. Shimomura, T. Yoshioka, and T. Tsuru, *AIChE J.* 2011, **57**, 2755-2765